Conformations of Cyclopentasilane Stereoisomers Control Molecular Junction Conductance

Haixing Li,[1] Marc H. Garner,[2] Zhichun Shangguan,[3] Timothy A. Su,[4] Madhav Neupane,[4] Panpan Li,[3] Alexandra Velian,[4] Michael L. Steigerwald,[4] Shengxiong Xiao,*[3] Colin Nuckolls,*[3,4] Gemma C. Solomon,*[2] Latha Venkataraman*[1,4]

[1] Department of Applied Physics and Applied Mathematics, Columbia University, New York 10027, USA

[2] Nano-Science Center and Department of Chemistry, University of Copenhagen, Universitetsparken 5, 2100 Copenhagen Ø, Denmark

[3] The Education Ministry Key Lab of Resource Chemistry, Shanghai Key Laboratory of Rare Earth Functional Materials, Optoelectronic Nano Materials and Devices Institute, Department of Chemistry, Shanghai Normal University, Shanghai 200234, China

[4] Department of Chemistry, Columbia University, New York 10027

Table of Contents

I. Synthetic procedures and characterization of compounds

All reactions were performed in an oven-dried or flame-dried round bottom flask, unless otherwise noted. The flasks were fitted with rubber septa and reactions were conducted under a positive pressure of nitrogen or argon, unless otherwise noted. Anhydrous and anaerobic solvents were obtained from a PureSolv MD5 solvent purification system. Commercial reagents were used without further purification. Silicon tetrachloride and 18-crown-6 were purchased from Aladdin Reagent. Tetrahydrofuran and potassium tert-butoxide were purchased from J&K Chemical Ltd. Lithium granules were purchased from Alfa Aesar. Toluene was purchased from Sigma-Aldrich. All other chemicals were purchased from TCI.

^{1}H, ^{13}C, and ^{29}Si NMR spectra were recorded on a Bruker DRX300 (300 MHz), Bruker DRX400 (400 MHz), or a Bruker DMX500 (500 MHz) spectrometer. Chemical shifts for protons are reported in parts per million downfield from tetramethylsilane and are referenced to residual protium in the NMR solvent (CHCl$_3$: δ 7.26). Chemical shifts for carbon are reported in parts per million downfield from tetramethylsilane and are referenced to the carbon resonances of the solvent (CDCl$_3$ δ 77.16). Chemical shifts for silicon are reported in parts per million downfield from tetramethylsilane and referenced to the silicon resonance of tetramethylsilane (TMS δ 0.0). Data are represented as follows: chemical shift (δ in ppm), multiplicity (s = singlet, d = doublet), and integration. The mass spectroscopic data were obtained at the Columbia University mass spectrometry facility using a Waters XEVO G2XS QToF mass spectrometer equipped with a UPC2 SFC inlet, electrospray ionization (ESI) probe, atmospheric pressure chemical ionization (APCI) probe, and atmospheric solids analysis probe (ASAP).

Tetrakis(trimethylsilane)silane **1**
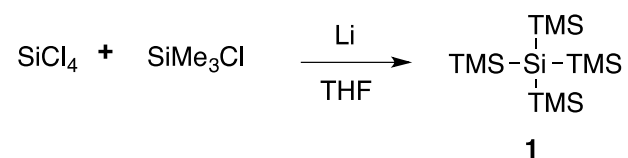
A three-necked flask was equipped with a dropping funnel, a reflux condenser, and a thermometer. The dropping funnel was charged with a mixture of tetrachlorosilane (79.0 g, 0.465 mol, 1.00 equiv.) and chlorotrimethylsilane (247.6 g, 2.28 mol, 4.90 equiv.). The flask was charged with lithium shot (27.1 g, 3.91 mol, 8.40 equiv.) and tetrahydrofuran (THF, 560 mL). The flask was cooled to 0°C with an ice-water bath and the mixture of chlorotrimethylsilane and tetrachlorosilane from the dropping funnel was added

dropwise to the flask over 6 hours. During addition, a gold-brown suspension formed. The reaction was stirred for 16 h at room temperature, refluxed for 2 h, quenched with water and extracted with hexanes. The organic layer was separated, dried over Na_2SO_4 and concentrated *in vacuo*. Recrystallization from ethanol yielded tetrakis(trimethylsilyl)silane **1** as a white solid (104 g, 70% yield). The NMR characterization matches previous reports from the literature.[1]

2,2,3,3-tetramethyl-1,1,1,4,4,4-hexakis(trimethylsilyl)tetrasilane 2
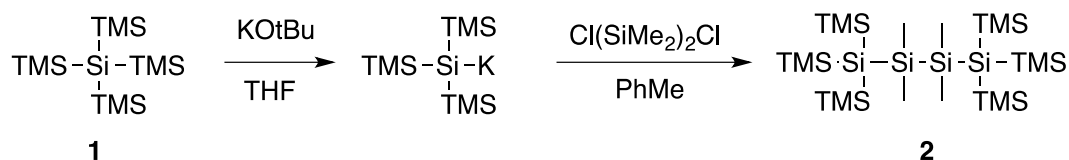
This procedure was adapted from the literature.[2] At room temperature, **1** (20.0 g, 62.3 mmol, 2.00 equiv.) and potassium tert-butoxide (7.34 g, 65.4 mmol, 2.10 equiv.) were mixed together in a flask with 60 ml THF. The solution immediately adopted a yellow color. The mixture was then stirred overnight. The THF was removed *in vacuo* and toluene (80 mL) was subsequently added. The reaction mixture was cooled to -78 °C with a dry ice-acetone bath and 1,2-dichlorotetramethyldisilane (5.83 g, 31.2 mmol, 1.00 equiv.) in toluene (40 mL) was added over 30 min. After stirring for 2 h at room temperature, the reaction mixture was subjected to an aqueous workup with 2 M H_2SO_4, extracted with diethyl ether, then dried over sodium sulfate. After removal of the solvent, the white residue was recrystallized from acetone/ether to obtain **2** as a white solid (16.2 g, 26.5 mmol, 85% yield). The NMR characterization matches previous reports from the literature.[2]

1,1,3,3-tetrakis(trimethylsilyl)hexamethylcyclopentasilane 3
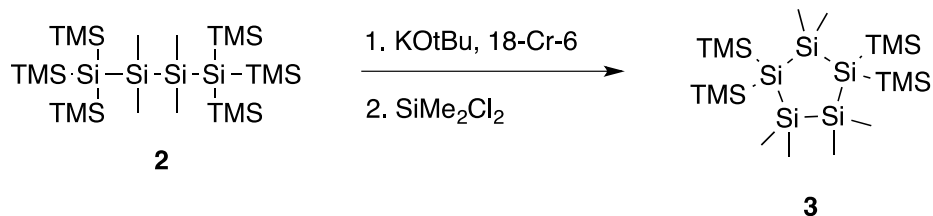
At room temperature, **2** (10.0 g, 16.4 mmol, 1.00 equiv.), potassium tert-butoxide (3.68 g, 32.8 mmol, 2.00 equiv.) and 18-crown-6 (8.66 g, 32.8 mmol, 2.00 equiv.) were mixed with toluene (60 mL). Immediately the solution turned orange. After stirring overnight, a solution of dichlorodimethylsilane (2.12 g, 16.4 mmol, 1.00 equiv.) in toluene (10 mL) was added dropwise to the reaction mixture. After complete addition, the orange

color of the silyl potassiate vanished and the reaction mixture turned colorless. The reaction mixture was then stirred at r.t. for 4 h and subjected to an aqueous workup with toluene and 2 M H_2SO_4. After removal of the solvent, the white residue was recrystallized from acetone/ ether to obtain **3** as a white solid (6.95 g, 13.3 mmol, 81% yield). The NMR characterization matches previous reports from the literature.[3, 4]

trans-Si5 and cis-Si5

At room temperature, **3** (500 mg, 0.96 mmol, 1.00 equiv.), tert-BuOK (214 mg, 1.91 mmol, 2.00 equiv.), and 18-crown-6 (505 mg, 1.91 mmol, 2.00 equiv.) were dissolved in 5 mL toluene. Immediately the solution turned orange and the solution was stirred overnight. ClCH$_2$SMe was added dropwise to the reaction mixture, after which the solution turned colorless. The reaction mixture was stirred at r.t. for 4 h and subjected to an aqueous workup with 2 M H_2SO_4 followed by extraction with toluene. After removal of the solvent, the crude residue was purified by silica gel chromatography with hexanes as eluent, and the following stereoisomers were separated.

trans-Si5: colorless oil (10 % yield). ^{1}H NMR (CDCl$_3$, 500 MHz) δ 2.14 (s, 6H), 1.99 (s, 2H), 1.96 (s, 2H), 0.39 (s, 6H), 0.28 (s, 6H), 0.27 (s, 6H), 0.25 (s, 18H). ^{13}C NMR (126 MHz, CDCl$_3$) δ 21.99, 15.36, 1.72, -1.38, -3.17, -4.48. ^{29}Si NMR (60 MHz, CDCl$_3$) δ -9.86 , -28.66 , -33.15 , -75.68. HRMS (TOF MS ASAP+) for $C_{16}H_{46}S_2Si_7$: calculated = 499.1504 found = 499.1492 (M+).

cis-Si5: white solid (15 % yield). ^{1}H NMR (CDCl$_3$, 500 MHz) δ 2.16 (s, 6H), 2.08 (d, J=11.5 Hz, 2H), 2.05 (d, J=11.0 Hz, 2H), 0.45 (s, 3H), 0.33 (s, 6H), 0.28 (s, 3H), 0.24 (s, 18H), 0.23 (s, 6H). ^{13}C NMR (126 MHz, CDCl3) δ 22.06, 15.45, 1.75, -0.45, -2.22, -3.39, -4.30. ^{29}Si NMR (60 MHz, CDCl$_3$) δ -9.66, -28.61, -32.68, -74.87. HRMS (TOF MS ASAP+) for $C_{16}H_{46}S_2Si_7$: calculated = 499.1504 found = 499.1496 (M+).

II. STM-Break Junction experiment details

We measured the conductance of single molecules bound to gold electrodes using a home-built modified Scanning Tunneling Microscope (STM). We used a 0.25 mm diameter gold wire (99.998%, Alfa Aesar) as the STM tip and a gold—coated (99.999%, Alfa Aesar) mica surface as the substrate. A commercially available single-axis

piezoelectric positioner (Nano-P15, Mad City Labs) was used to achieve sub-angstrom level control of the tip-substrate distance. The STM was controlled using a custom written program in IgorPro (Wavemetrics, Inc.) and operated in ambient conditions at room temperature. The gold substrate was cleaned using UV/Ozone for 15 minutes prior to use. For each measurement, 1000 traces were first collected prior to adding molecular solutions to ensure that the gold was clean. Solutions of the target molecules at 1 mM concentration in 1,2,4-trichlorobenzene (Sigma-Aldrich or Alfa Aesar, 99% purity) were added to the substrate for molecular conductance measurements. The applied bias was 225 mV, and the substrate was displaced at a speed of 19 nm/s for all measurements. The current and voltage data were acquired at 40 kHz. For each molecule, we collected over 10,000 traces to create 1D and 2D conductance histograms without data selection (Figure 2 in the main text).

III. Additional Data
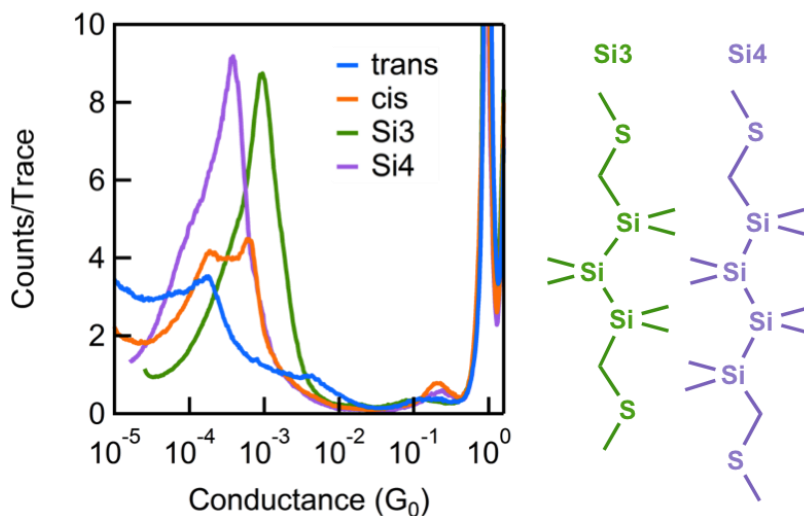
Figure S1. Logarithmically binned 1D conductance histogram of **cis-Si5** (orange), **trans-Si5** (blue), **Si3** (green) and **Si4** (purple). Histograms are made without data selection and normalized by the total number of traces.
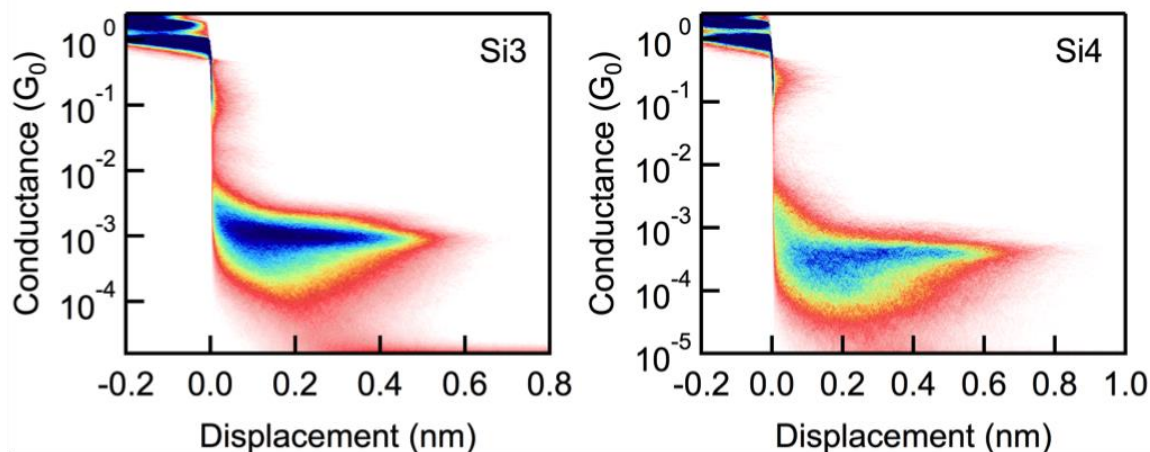
Figure S2. *2D conductance histograms of **Si3** and **Si4**. 2D histograms are created by overlaying all conductance traces after aligning them to zero-displacement at the point when the conductance crosses $0.5G_0$.*

IV. Computational Details

1. Conformational Study and Nomenclature

As described in the manuscript, we find 86 conformers of **trans-Si5** and 84 conformers of **cis-Si5**. Though the energy barriers between the conformers may be small in many cases[16], we think the large number of conformers is a testament to the vast structural variation and flexibility of cyclic silanes.

The initial structure for each conformer was created with Avogadro[5] and partially relaxed with the MMFF94 force field[6-10] to create a realistic starting-guess for the DFT optimization. Following the optimization, we assessed the structures to see whether they still correspond to the conformer of the provisional structure. We have systematically determined whether a conformer is a twist (C_2) or an envelope (C_s), however, the CH₂-SMe linkers and TMS substituents are bulky and cause steric distortion on the ring. The conformers we find therefore diverge, in some cases considerably, from the idealized conformations of C_s and C_2 symmetry. Generally, we consider a structure an envelope conformer if one of the Si—Si—Si—Si dihedrals is smaller than 5°, thus forming a four-atom plane. With this definition, any conformation that is not an envelope is defined as a twist, given there will always be three atoms in plane.

We have adapted the nomenclature that was previously used in the literature[16], but the twist conformation has also been referred to as twist-envelope[17] and half-chair[18]. To the best of our knowledge, there is no convention for systematically naming the conformers of di-substituted five-membered rings. As an example, the name **1-twist-a1**

starts with the label of the ring conformation "**1-twist**", followed by a letter "**a**" indicating the side of the substituents relative to the ring and a serial number "**1**" for the linker orientation. There are four different letters that can appear after "twist" or "envelope" in the name: for envelope conformers **b** represents 'back-side' and **f** represents 'front-side' (of the "envelope"); for twist conformers **e** represents 'equatorial' and **a** represents 'axial'. The name ends with a serial number: 1-4 represent conformers with both sulfurs pointing away from the ring, numbers 5-8 represent one sulfur pointing towards the ring and one pointing away, and number 9 represents both sulfurs point into the ring.

2. Vacuum Boltzmann Populations

The energies and Boltzmann populations at 300K are listed in **Table S1** and **S2**. The energies are the uncorrected 0 K energies. All structures listed in **Table S1** and **S2** are included as 3D-rotable web-enhanced objects in xyz file format.

Table S1. Boltzmann distribution of ***cis-Si5*** in vacuum. Energy is relative to the most stable conformer (1—twist—e7).

Conformer	E (eV)	Degeneracy	P(300K)
1-twist-a1	0.05	2	2.1%
1-twist-a2	0.07	2	0.9%
1-twist-a3	0.08	2	0.7%
1-twist-a4	0.06	2	1.1%
1-twist-a5	0.04	2	2.6%
1-twist-a6	0.04	2	2.5%
1-twist-a7	0.07	2	0.8%
1-twist-a8	0.05	2	1.7%
1-twist-e1	0.04	2	3.3%
1-twist-e2	0.00	2	11.2%
1-twist-e3	0.05	2	2.0%
1-twist-e4	0.03	2	3.7%
1-twist-e5	0.13	2	0.1%
1-twist-e6	0.11	2	0.2%
1-twist-e7	**0.00**	**2**	**13.3%**
1-twist-e8	0.03	2	4.3%
1-twist-e9	0.12	2	0.1%
1-envelope-b1	0.08	2	0.7%
1-envelope-b2	0.10	2	0.3%
1-envelope-b3	0.08	2	0.5%
1-envelope-b4	0.11	2	0.2%

1-envelope-b5	0.04	2	2.8%
1-envelope-b6	0.04	2	2.9%
1-envelope-b7	0.10	2	0.3%
1-envelope-b8	0.12	2	0.2%
1-envelope-b9	0.20	2	0.0%
1-envelope-f1	0.10	2	0.3%
1-envelope-f2	0.12	2	0.1%
1-envelope-f3	0.08	2	0.7%
1-envelope-f4	0.09	2	0.3%
1-envelope-f5	0.21	2	0.0%
1-envelope-f6	0.21	2	0.0%
1-envelope-f9	0.26	2	0.0%
4-envelope-b1	0.07	2	0.8%
4-envelope-b2	0.06	2	1.2%
4-envelope-b3	0.06	2	1.5%
4-envelope-b4	0.05	2	2.1%
4-envelope-b5	0.18	2	0.0%
4-envelope-b6	0.16	2	0.0%
4-envelope-b7	0.05	2	2.1%
4-envelope-b8	0.05	2	1.6%
4-envelope-b9	0.14	2	0.1%
4-envelope-f1	0.04	2	2.7%
4-envelope-f2	0.15	2	0.0%
4-envelope-f3	0.07	2	0.9%
4-envelope-f4	0.09	2	0.4%
4-envelope-f5	0.03	2	4.6%
4-envelope-f6	0.03	2	3.6%
4-envelope-f7	0.11	2	0.2%
4-envelope-f8	0.14	2	0.1%
4-envelope-f9	0.15	2	0.0%
4-twist-a1	0.09	2	0.4%
4-twist-a2	0.12	2	0.1%
4-twist-a3	0.11	2	0.2%
4-twist-a4	0.09	2	0.5%
4-twist-a5	0.08	2	0.7%
4-twist-a6	0.05	2	1.7%
4-twist-a7	0.10	2	0.3%

4-twist-a8	0.08	2	0.6%
4-twist-e1	0.10	2	0.2%
4-twist-e3	0.08	2	0.5%
4-twist-e4	0.09	2	0.5%
4-twist-e5	0.20	2	0.0%
4-twist-e8	0.19	2	0.0%
2-envelope-f1	0.08	2	0.6%
2-envelope-f2	0.11	1	0.1%
2-envelope-f3	0.10	1	0.1%
2-envelope-f4	0.09	2	0.5%
2-envelope-f5	0.06	2	1.5%
2-envelope-f6	0.21	1	0.0%
2-envelope-b1	0.06	2	1.5%
2-envelope-b2	0.11	1	0.1%
2-envelope-b3	0.06	1	0.8%
2-envelope-b4	0.18	2	0.0%
2-envelope-b5	0.16	2	0.0%
2-envelope-b6	0.27	1	0.0%
2-twist-1	0.07	2	0.8%
2-twist-2	0.06	2	1.3%
2-twist-3	0.09	2	0.5%
2-twist-4	0.08	2	0.7%
2-twist-6	0.03	2	3.8%
2-twist-7	0.14	2	0.1%
2-twist-8	0.16	2	0.0%
2-twist-9	0.14	2	0.1%

Table S2. *Boltzmann distribution of the **trans-Si5** in vacuum. Energy is relative to the most stable conformer (1—envelope—b3).*

Conformer	E (eV)	Degeneracy	P(300K)
1-envelope-b1	0.08	2	1.0%
1-envelope-b2	0.08	2	0.8%
1-envelope-b3	**0.00**	**2**	**20.9%**
1-envelope-b4	0.02	2	9.3%
1-envelope-b5	0.09	2	0.7%

1-envelope-b6	0.03	2	6.3%
1-envelope-b7	0.12	2	0.2%
1-envelope-b8	0.08	2	0.9%
1-envelope-f1	0.05	2	3.0%
1-envelope-f2	0.06	2	1.9%
1-envelope-f3	0.06	2	2.3%
1-envelope-f4	0.05	2	2.5%
1-envelope-f5	0.13	2	0.1%
1-envelope-f6	0.17	2	0.0%
1-envelope-f7	0.13	2	0.2%
1-envelope-f8	0.08	2	0.9%
1-envelope-f9	0.16	2	0.0%
1-twist-a1	0.10	2	0.4%
1-twist-a2	0.13	2	0.1%
1-twist-a3	0.08	2	1.0%
1-twist-a4	0.10	2	0.5%
1-twist-a5	0.12	2	0.2%
1-twist-a6	0.08	2	0.9%
1-twist-a7	0.13	2	0.1%
1-twist-a8	0.10	2	0.4%
1-twist-e1	0.06	2	2.1%
1-twist-e2	0.05	2	3.6%
1-twist-e3	0.08	2	1.1%
1-twist-e4	0.05	2	3.0%
1-twist-e5	0.14	2	0.1%
1-twist-e6	0.17	2	0.0%
1-twist-e7	0.11	2	0.3%
1-twist-e8	0.07	2	1.5%
1-twist-e9	0.19	2	0.0%
2-envelope-1	0.05	2	3.2%
2-envelope-2	0.12	2	0.2%
2-envelope-3	0.06	2	2.0%
2-envelope-4	0.14	2	0.1%
2-envelope-5	0.10	2	0.4%
2-envelope-6	0.19	2	0.0%
2-envelope-7	0.11	2	0.3%
2-envelope-8	0.19	2	0.0%
2-envelope-9	0.11	2	0.3%

2-twist-u1	0.09	2	0.8%
2-twist-u2	0.09	2	0.6%
2-twist-u3	0.09	2	0.6%
2-twist-u4	0.16	2	0.0%
2-twist-u5	0.15	2	0.1%
2-twist-u6	0.22	2	0.0%
2-twist-d1	0.14	2	0.1%
2-twist-d2	0.13	2	0.1%
2-twist-d3	0.16	2	0.0%
2-twist-d4	0.12	2	0.2%
2-twist-d5	0.12	2	0.2%
2-twist-d6	0.06	2	2.0%
4-envelope-b1	0.11	2	0.3%
4-envelope-b2	0.12	2	0.2%
4-envelope-b3	0.12	2	0.2%
4-envelope-b4	0.12	2	0.2%
4-envelope-b5	0.15	2	0.1%
4-envelope-b6	0.15	2	0.1%
4-envelope-b7	0.20	2	0.0%
4-envelope-b8	0.21	2	0.0%
4-envelope-b9	0.25	2	0.0%
4-envelope-f1	0.12	2	0.2%
4-envelope-f2	0.11	2	0.4%
4-envelope-f3	0.09	2	0.6%
4-envelope-f4	0.11	2	0.4%
4-envelope-f5	0.09	2	0.6%
4-envelope-f6	0.09	2	0.6%
4-envelope-f7	0.09	2	0.6%
4-envelope-f8	0.07	2	1.4%
4-envelope-f9	0.04	2	4.1%
4-twist-e1	0.04	2	4.3%
4-twist-e2	0.08	2	1.1%
4-twist-e3	0.06	2	1.9%
4-twist-e4	0.07	2	1.4%
4-twist-e5	0.17	2	0.0%
4-twist-e6	0.13	2	0.1%
4-twist-e8	0.10	2	0.5%

4-twist-a1	0.11	2	0.4%
4-twist-a2	0.13	2	0.2%
4-twist-a3	0.07	2	1.5%
4-twist-a4	0.09	2	0.8%
4-twist-a7	0.18	2	0.0%
4-twist-a8	0.13	2	0.1%

As the molecule is sterically congested, the lack of proper treatment of dispersion interaction with the PBE functional may influence the results. To test this, the Van der Waals correction to the vacuum energy suggested by Tkatchenko and Scheffler[11] (TS09) is applied. The vacuum energies of the 20 highest population conformers of each isomer are included in table S3 and S4. In general, the relative energies are switched systematically. The energy differences between the conformers become larger, and as a result the Boltzmann population changes. However, as the change is fairly systematic it only has minor effect on our analysis of the transmission results. In Figure S3, the TS09 dispersion corrected energies and vacuum populations are plotted. Compared to its equivalent figure in the figure 5a in the manuscript, the peak shape in panel *a* changes but is qualitatively very similar, while panel *b* is almost unaffected by the correction. Therefore we proceed with the non-corrected energies in manuscript, noting that although our results are subject to the method, the conclusions remain unaffected.

Table S3. *Boltzmann distribution of the 20 highest populated conformers of* **cis-Si5** *in vacuum. Uncorrected energies are the energies from table S1 (PBE with no correction). Corrected energies are calculated with PBE and the TS09 correction scheme. Energy is relative to the most stable conformer (1—twist—e7).*

Conformer	$E_{uncorrected}$ (eV)	$E_{corrected}$ (eV)	P(300K)
1-twist-e7	0.00	0.00	20.3%
1-twist-e2	0.00	0.02	11.0%
1-twist-e8	0.03	0.03	6.3%
4-envelope-f6	0.03	0.04	4.6%
4-envelope-f5	0.03	0.04	4.6%
2-twist-6	0.03	0.04	4.5%
1-twist-e4	0.03	0.04	3.6%
1-envelope-b6	0.04	0.04	3.6%

1-twist-a8	0.05	0.05	3.2%
4-envelope-b7	0.05	0.05	3.1%
1-twist-a7	0.07	0.05	2.8%
1-twist-a6	0.04	0.05	2.7%
1-twist-e1	0.04	0.05	2.7%
4-envelope-b8	0.05	0.06	2.1%
1-twist-a1	0.05	0.06	2.1%
1-envelope-b5	0.05	0.06	2.1%
1-twist-a5	0.04	0.06	1.9%
4-twist-a6	0.05	0.06	1.7%
1-twist-e3	0.05	0.07	1.2%
4-envelope-b4	0.05	0.07	1.1%

Table S4. *Boltzmann distribution of the 20 highest populated conformers of* **trans-Si5** *in vacuum. Uncorrected energies are the energies from table S2 (PBE with no correction). Corrected energies are calculated with PBE and the TS09 correction scheme. Energy is relative to the most stable conformer (1—envelope—b3).*

Conformer	$E_{uncorrected}$ (eV)	$E_{corrected}$ (eV)	P(300K)
1-envelope-b3	0.00	0.00	32.1%
1-envelope-b4	0.02	0.02	12.3%
4-envelope-f9	0.04	0.04	6.0%
1-envelope-b6	0.03	0.04	5.7%
4-twist-e1	0.04	0.06	3.0%
2-envelope-1	0.05	0.06	2.7%
2-twist-d6	0.06	0.07	2.6%
1-envelope-f1	0.05	0.07	2.4%
1-envelope-f4	0.05	0.07	2.1%
1-twist-e2	0.05	0.07	2.1%
1-envelope-b8	0.08	0.07	1.9%
1-twist-e1	0.06	0.07	1.9%
4-twist-a3	0.07	0.07	1.9%
4-twist-e3	0.06	0.07	1.8%
2-envelope-3	0.06	0.08	1.7%
1-envelope-f3	0.06	0.08	1.5%
1-twist-e8	0.08	0.08	1.4%
1-twist-e4	0.05	0.08	1.4%
1-twist-a3	0.08	0.09	1.2%
1-envelope-f2	0.06	0.09	1.0%
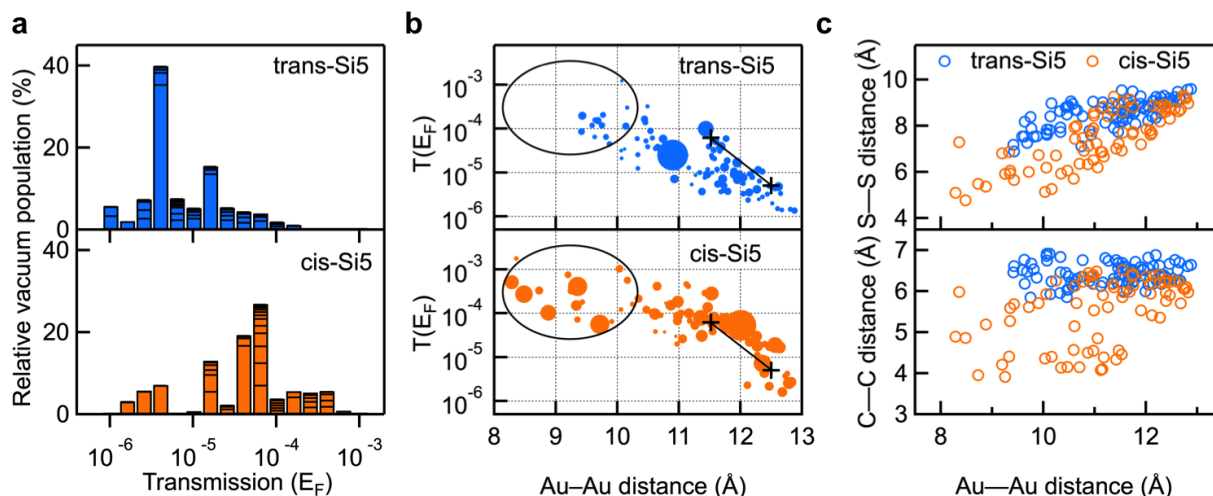
Figure S3. Equivalent to figure 5 in the manuscript but the dispersion corrected energies (and populations) for all conformers are used. Caption of Figure 5 follows here: Logarithmically binned histogram of transmission at Fermi energy of the 91 trans-Si5 and 74 cis-Si5 conformers. The horizontal stack lines in the bars indicate the vacuum population of each conformer. The histogram is normalized to sum up to 100%. (b) Transmission at Fermi energy plotted against the Au—Au junction distance for each trans-Si5 and cis-Si5 conformer bridged between four-atom Au pyramids. For easier visualization, the size of each dot has been scaled by $1/(1+E)$, where E is the relative vacuum energy of each conformer in units of kT at 300K, see table S1 and S2 in SI. Black ⬚ are the calculated transmissions for the two configurations of the linear Si3 with both terminal Au—S—CH2—Si dihedrals in ortho conformations. Black circles and lines highlight the difference between the two isomers. (c) S—S (upper panel) and C—C junction distance (lower panel) plotted against the Au—Au junction distance for each trans-Si5 and cis-Si5 conformer. S refers to sulfur; C refers to the CH2-group that bridges the silicon ring and the methylsulfide group. All three plots share the same color scheme: orange for cis-Si5 and blue for trans-Si5.

3. Creating junction structures

To capture the large structural variation for non-rigid saturated molecules when calculating the transmission, we created a full set of junctions based on the optimized vacuum structures. We built junctions based on idealized contact geometries and optimized the junction before calculating the transmission.

Below we describe the automated procedure for generating a large number of junctions in a systematic way from a set of vacuum conformers.

1. The optimized vacuum structure is loaded into the Atomic Simulation Environment.
2. For each sulfur, an Au atom is placed in the transoid (±170°) or ortho (±90°) dihedral position, with a C—S—Au angle of 110° and a S—Au distance of 2.525 Å (transoid) or 2.55 Å (ortho) as shown in Figure S4. With the Au atom in transoid position, the terminal methyl groups are rotated to the opposite ortho position.
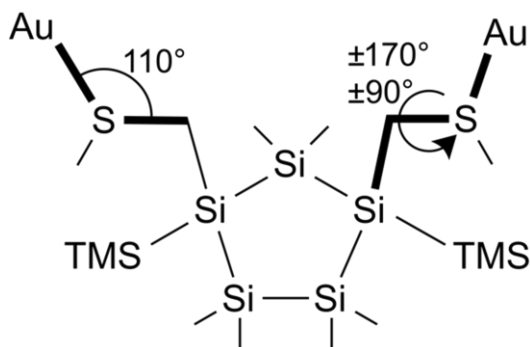
Figure S4: Schematic of the molecule and the initial positions of the tip Au-atoms.

3. Three Au atoms are placed 'below' the Au tip atoms, along the Au—Au axis (defined as the z-axis), and furthermore a 4×4×4 Au(111) fcc slab is placed under one of the pyramids as shown in Figure S5.

Figure S5: Example of an initial junction structure with unit cell.

4. The molecule is rotated around the Au—Au axis to the position where the terminal methyl groups are furthest away from the nearest two Au atoms at the bottom of the Au pyramids, thereby giving the initial structure the least steric tension at the contact.
5. A series of tests are run to determine if the initial junction structure is feasible. Most notably the Au—Au distance must be at least 8 Å, and no atom in the molecule is within 1.8 Å distance to the Au atoms.
6. All possible combinations of conformers (170) and junction contact geometries (16 per conformer) are created. Among the 2720 possible initial junctions, the ones that pass the test are created and relaxed with periodic boundary conditions in all three dimensions, the bottom of the Au slab is thus effectively the top of the junction. All Au-atoms are kept fixed during the optimization.

7. Following the relaxation, the final structure is tested to make sure that the molecule has not left the Au contact (we use a threshold of 2.8 Å for the Au—S distance). If the molecular conformation has changed into another one during the process, the final structure is also discarded.

This procedure leaves us 490 optimized junctions. All structures are included as 3D-rotable web-enhanced objects in xyz file format.

211 of the *cis* isomer

- 74 with both Au atoms in ortho con5uration.
- 98 with one Au in ortho and one in anti configuration.
- 39 with both Au atoms in anti configuration.

279 of the *trans* isomer

- 91 with both Au atoms in ortho configuration.
- 140 with one Au in ortho and one in anti configuration.
- 48 with both Au atoms in anti configuration.

We calculate the transmission for all these junctions as described in the manuscript. We note that for the transmission calculation, we place Au slabs on both sides of the junction and only use periodic boundary conditions in the *x* and *y* directions.

4. Comparison of linear and cyclic systems: junction geometries and transmission

Cyclic systems are structurally very different from linear systems. In cyclic systems certain dihedral angles are inherently constrained to a limited range, which gives rise to a large number of conformers with rather similar spatial structure. Linear systems also have large conformational freedom, but the all-anti/all-transoid conformations dominate at room temperature.[12, 13] From a structural point of view these conformers are excellent for forming junctions. The terminal methyl groups are positioned such that the sulfur atoms are generally quite unprotected as shown in **Figure S6B and S6C,** where junctions of linear **Si3** and **Si4** are shown with the Au atoms in ortho and anti configurations. When both the terminal dihedrals are in the ortho configuration, the junction is around 2 Å shorter than the anti configuration, in good agreement with previous experiments.[14] We note that for the linear structures, we have constrained the backbone to the all-anti configuration; their transmissions are plotted in **Figure S7**. The unconstrained all-transoid structures are very similar with almost identical Au—Au length and transmission.

Why focus the analysis on junctions with the terminal Si—CH$_2$—S—Au dihedrals in the ortho configuration, when the anti configuration is predominantly observed for linear systems?

In the manuscript the analysis of the computational results is focused solely on junctions with contact geometry in ortho configuration. As will be discussed in the part 6 of this section, we see the clearest transmission difference between **cis-Si5** and **trans-Si5** for the data with the ortho/ortho contact geometry, however we emphasize that this is not the reason behind our choice.

The backbone dihedrals of cyclic systems are constrained and as a result an all-anti path can never be achieved for a stable conformation. In many of the highly populated conformers, e.g. cis—1—twist—e2 shown in **Figure S9C**, one or both Si—SiMe$_2$—Si—CH$_2$ backbone dihedrals are in ortho or gauche configurations. The cyclic systems that are closest to the all-anti configuration have backbone dihedrals constrained around 140°. Cis—1—twist—e3, in **Figure S6A**, is an example with Si—SiMe$_2$—Si—CH$_2$ dihedrals of 141° and 125°. This makes the S—S distance of the cyclic silanes shorter than a linear all-anti chain. However, the ortho positions of the terminal dihedrals almost point along the S—S axis of the molecule, thus making the Au—Au distance almost as long as all-anti **Si3** in some cases. For cyclic systems, both terminal methyl dihedrals in anti configuration can sometimes result in shorter S—S distance. These are direct structural consequences of rotating dihedrals for tetrahedral bonds, and can be recognized by comparing the positions of the terminal methyl groups and Au atoms relative to the sulfur atoms in the structures in **Figure S6**.
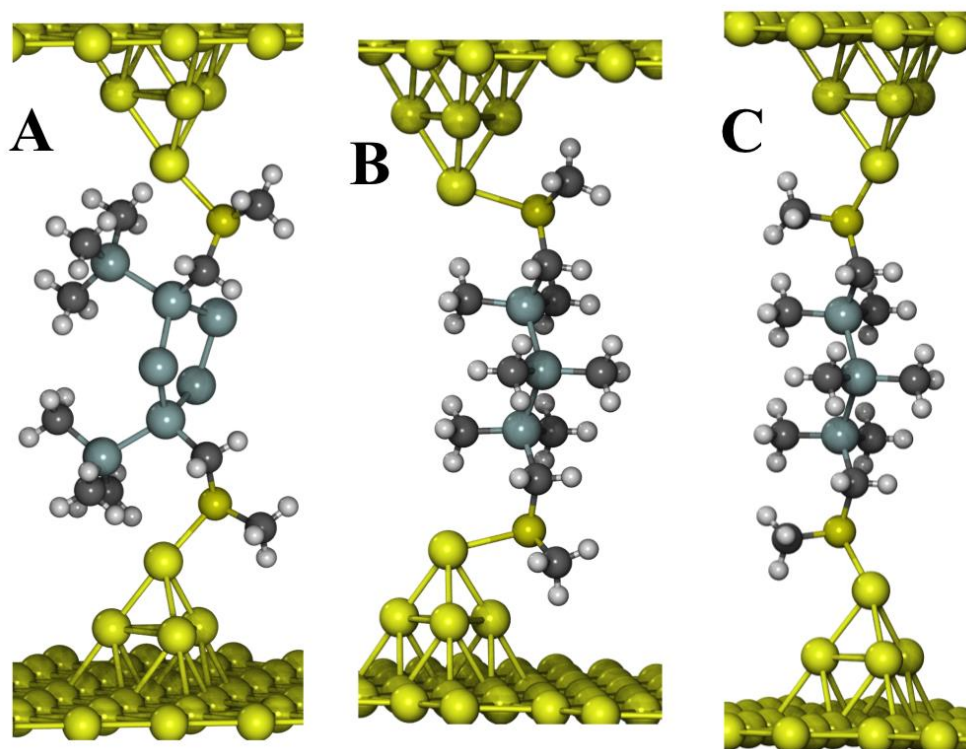
Figure S6. *Structures of relaxed junctions.* **A**: *cis—1—twist—e3, vac. pop: 2.0%, methyl groups on the ring are removed for clarity. Au—Au distance: 12.8 Å.* **B**: *Linear Si3 with terminal Si—C—S—Au dihedrals in ortho configuration. Au—Au distance: 11.5 Å.* **C**: *Linear Si3 with terminal Si—C—S—Au dihedrals in anti configuration. Au—Au distance: 13.6 Å.*

In vacuum, the terminal methyl groups in anti position are the most stable configuration. The 'initial' junction configuration is likely with the Au atoms in ortho position and the terminal methyl groups in anti position. This is also why we think the terminal methyl group position is important for controlling junction formation as discussed in part 3 of this section.

A full assessment of the dynamics of contact geometries and how they can switch from one to the other is beyond the scope of this study. While we cannot rule out the possibility that one or both terminal dihedrals can be in anti configuration in the experiment, we think the ortho configuration is the majority. We emphasize that by mainly focusing on the ortho configuration, we are making an assumption that may restrict the broader applicability of these results.

Does the short or the long through-bond path dominate the transport in cyclic systems?

To support the analysis of the experimental data in the manuscript, we have calculated the transmission of linear **Si3** and **Si4**. The backbone dihedrals are varied systematically by applying a constraint in the optimization procedure. Otherwise the method is the same as for the cyclic systems. In **Figure S7A, C** one Si—SiMe$_2$—Si—CH$_2$ backbone dihedral is varied for **Si3**. The transmission is the highest for the anti configuration and decrease as the dihedral angle becomes smaller. When the terminal dihedral *Si—C—S—Au* is in the strongly coupled anti position the change in the transmission with the backbone dihedral is very systematic. When the dihedral *Si—C—S—Au* is in the weakly coupled ortho position the transmission is generally lower and the change is less systematic — probably because through-space coupling in the molecule becomes significant when the backbone transmission is low and the junctions are inherently shorter.

Similarly, the backbone Si—SiMe$_2$—SiMe$_2$—Si dihedral is varied for **Si4** in **Figure S7B, D**. The trend is comparable to the **Si3**, but the all-silicon dihedral seems to have a larger effect on the transmission. When the backbone dihedral is constrained to 60° or less, the transmission is lower than that for the **Si3**. Therefore we conclude that the long four-silicon path is not significant for the transmission in the cyclic system.

On the possible quantitative discrepancy between experiment and theory

In experiment, stereoelectronic conductance-switching was reported for a series of linear silanes, including **Si3** and **Si4**, with a switching ratio around a factor 2.[21] This was attributed to switching between the electrodes being in the ortho (low conductance) and anti (high conductance) configurations. However, the computational results discussed here show a much higher switching ratio: over an order of magnitude. A similar computational result recently published reported the same quantitative discrepancy using similar methods.[22] The transmission with the electrodes in anti configuration is slightly higher than reported in experiment (cf. Fig. S1 and S7). This is not surprising considering density functional theory is known to overestimate the transmission in π-conjugated molecules, primarily due to underestimating the HOMO-LUMO gap and poor energy-level alignment between the molecule and the electrodes.[23-25] However the weakly coupled ortho configuration has much lower transmission than the experimental values that were assigned to this configuration. It is important to keep in mind that it is unknown exactly what happens during the switching in experiment, for example it could be that the contact geometry at one end of the molecule changes. Still, this discrepancy does suggest that the transmission may be underestimated in the ortho-case. Such underestimation may be due to the effects that are not included in the theoretical approach, e.g. inelastic effects. This discrepancy however calls for caution in the analysis and remains as a topic for further investigation. As a consequence, we have not directly

compared the data for different contact geometries. The transmission data of junctions with ortho/ortho, anti/ortho, and anti/anti geometry are analyzed separately.
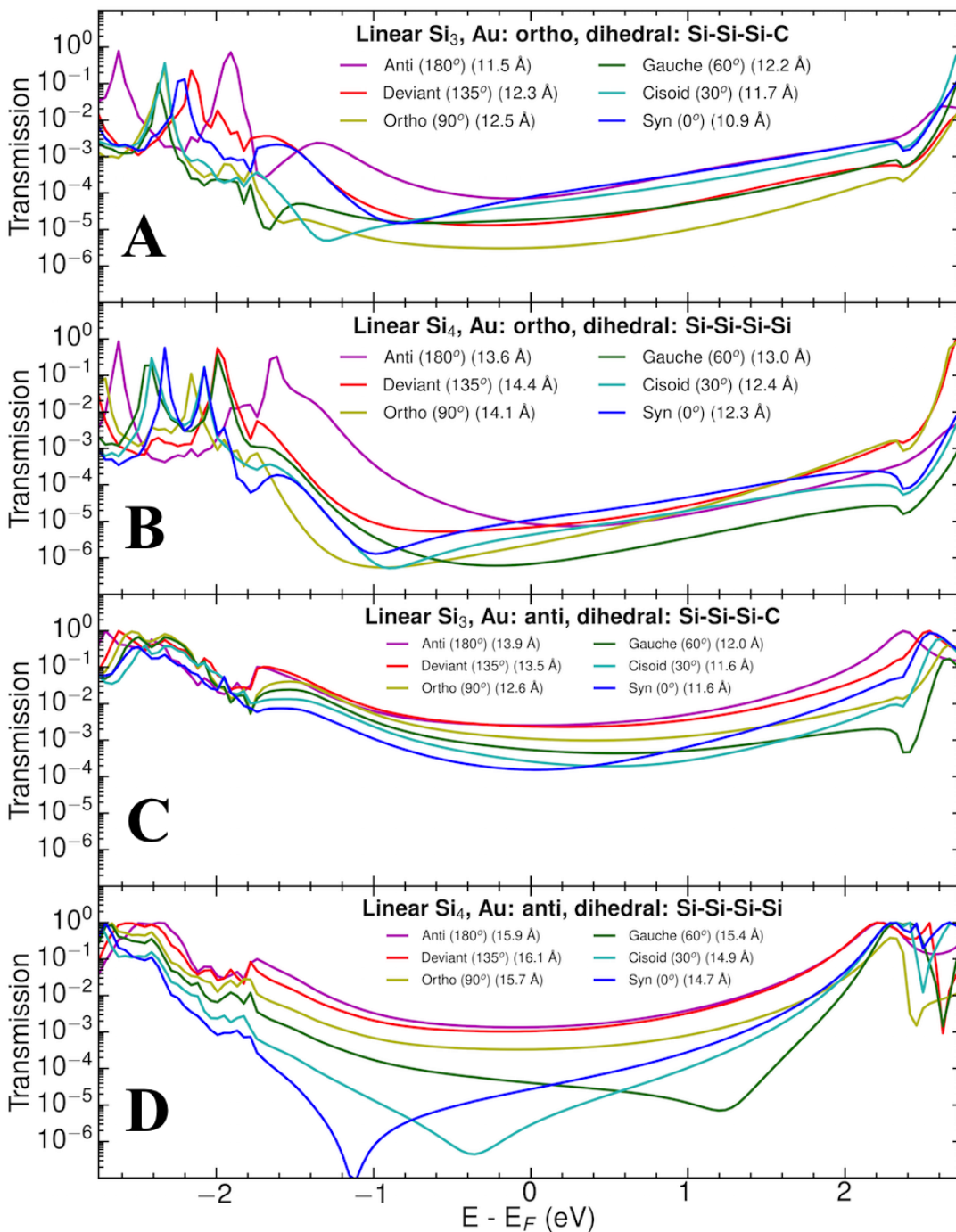

Figure S7. *Transmission calculated for linear (A, C)* ***Si₃*** *and linear (B, C)* ***Si₄*** *with terminal Si—CH₂—S—Au dihedrals in (A, B) ortho and (C, D) anti configurations. One of the Si— SiMe₂—Si—CH₂ dihedrals is varied systematically for* ***Si₃****, and the Si—SiMe₂—SiMe₂—Si dihedral is varied systematically for* ***Si₄*** *by fixing the dihedral during the optimization procedure. The Au—Au length of the junction is written in the legend. The relaxed junction*

structures of the 24 linear molecules are included as web-enhanced objects in xyz file format.

5. Analysis of vacuum structures

While the focus of our study is on the junction structures and the calculated transmission, we briefly highlight here some interesting trends in the vacuum structures.

As the transmission depends on the dihedrals along the molecular backbone, structural differences between the conformers of **cis-Si5** and **trans-Si5** may be the reason why **cis-Si5** has a higher conductance than **trans-Si5**.

In Figure S8 the vacuum populations of the significant dihedrals for the two possible pathways through the silicon backbone of **cis-Si5** and **trans-Si5** are plotted in histograms. In the top panel, the Si—Si—Si—Si dihedrals of the 4-atom silicon path are plotted and they are essentially the same for **cis-Si5** and **trans-Si5**. In both cases the dihedrals are always smaller than 50°, making the 4-atom path unfavorable for conductance.

In the middle panel, the sum of the two S—C—Si—Si linker dihedrals towards to the short 3-atom Si path is plotted. These dihedrals are not constrained by the ring structure and therefore adopt typical values for the tetrahedral structure of around 60° and 180°, which therefore sums to around 120°, 240° and 360°. Again the distribution is very similar for both **cis-Si5** and **trans-Si5**.

In the bottom panel, the sum of the two C—Si—Si—Si dihedrals of the 3-atom Si path is plotted. These dihedrals are constrained by the ring structure as well as the TMS groups and distribute over a range of different values depending on the conformation. The main peak of **cis-Si5** is slightly higher than the main peak of **trans-Si5**, however this is probably not enough to explain the notable difference in the measured conductance. Also the distribution is much wider for **cis-Si5**, making the result rather unclear. Even so, there is an indication that the conformers of **cis-Si5** may have somewhat more favorable dihedrals than **trans-Si5**.

An interesting conclusion from the experimental 1D and 2D conductance histograms is that **trans-Si5** appears to be less likely to form stable junctions compared to **cis-Si5**. While a number of different effects could come in play that we cannot readily assess, particularly the ones relating to the dynamics of junction formation and evolution. However, there is one structural trend we have found intriguing. Due to the structurally crowded nature of the molecule, we find the sulfurs mainly bind to the very under-

coordinated Au atoms. If we assume that the junctions form and evolve along the Au—Au axis, the molecule itself should not sterically block the sulfurs.
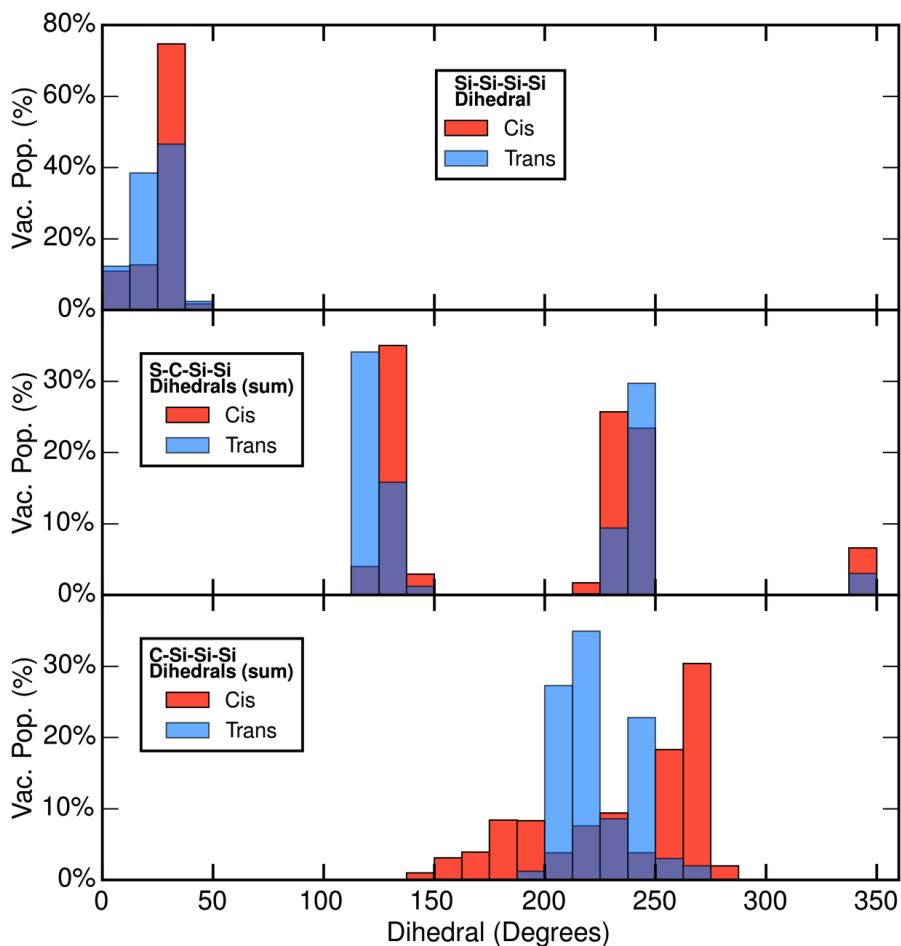

Figure S8: *Histogram of the vacuum populations of the dihedrals of the conformers. Top: Si—Si—Si—Si dihedral, the 'long' linker-to-linker path. Middle: Sum of both S—C—Si—Si linker dihedrals. Bottom: Sum of both C—Si—Si—Si dihedrals, the 'short' linker-to-linker path. All dihedrals are in absolute numbers (0-180°). Note trans is plotted in transparent blue on top of cis plotted in orange.*

The terminal methyl groups may often prevent effective junction formation or evolution. A simple way to assess if the positions of the terminal methyl groups are feasible is to use the through-space S—S—Me angle as exemplified in Figure S9a and S9b.
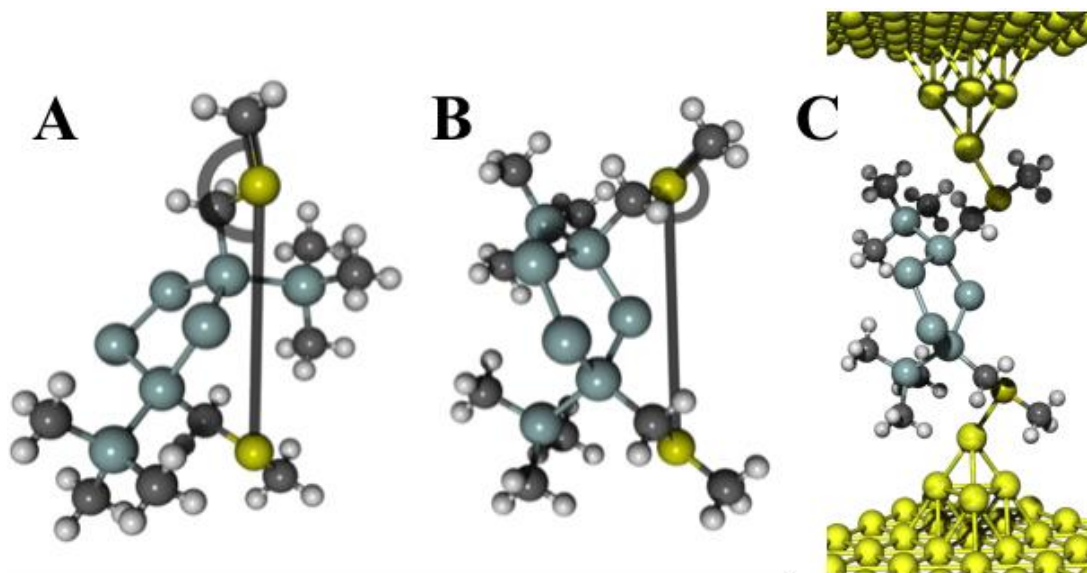
Figure S9: *Examples of vacuum and junction structures. Methyl groups on the ring have been removed for clarity.* *A:* *trans—1—envelope—b3 optimized in vacuum. One S—S—Me through-space angle is marked with a thick black line.* *B:* *cis—1—twist—e2 optimized in vacuum. One S—S—Me through-space angle is marked with a thick black line.* *C:* *cis—1— twist—e2 optimized in junction.*

If the S—S—Me angle is close to 180°, the methyl group is pointing along the S—S axis and will thus block the Au electrodes from binding to sulfur. An example of a conformer with an unfavorable S—S—Me angle is shown in Figure S9a where the vacuum structure of *trans—1—envelope—b3* is shown with one of its S—S—Me angles of 167.5°. If the angle is small the methyl group will point somewhat perpendicularly from the electrodes and the conformer may be able to effectively form a junction, as the sulfur is not sterically blocked. An example thereof is *cis—1—twist—e2* shown in Figure S9b. With both its S— S—Me angles being small (123.1° and 126.5°) it may be a more suitable conformer for effectively forming junctions.
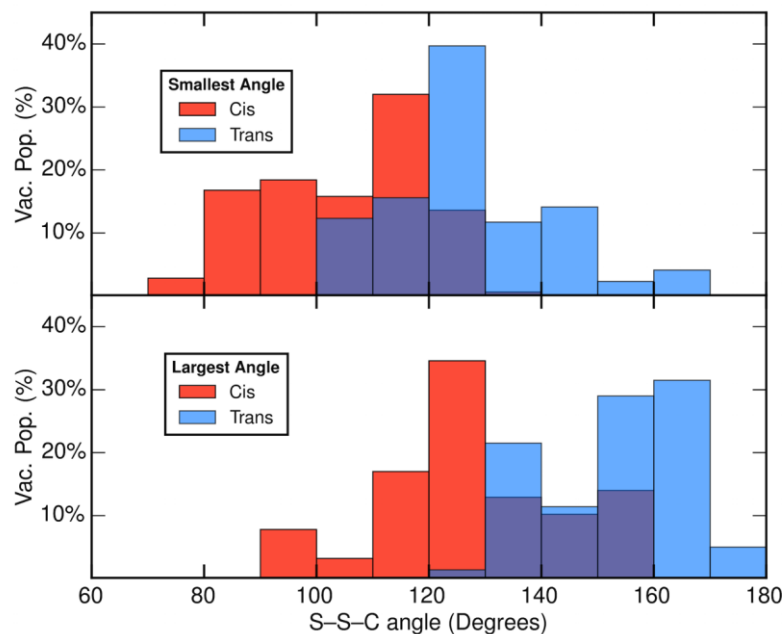
Figure S10: *Histogram of the vacuum populations of S—S—C (through-space) angles of the conformers. Top: Smallest of the two angles. Bottom: Largest of the two angles. Note that trans is plotted in transparent blue on top of cis plotted in orange.*

Now we compare the S—S—Me angle data for all conformers of cis-Si5 and trans-Si5 as shown in the population histograms in Figure S10. Because there are two angles and it is not obvious which one is more important for junction formation (if one angle is small and the other is large, presumably one sulfur may bind more easily than the other), we plot the smallest (top panel) and the largest (bottom panel) angles separately. In both cases trans-Si5 is distributed at bigger angles than cis-Si5. For the largest angle (bottom panel), trans-Si5 has the majority in the range of particular high values (around 150° and higher), which may considerably hinder effective junction formation. Although it is a simplified assessment of junction formation, it provides a well-reasoned structural argument for why the experimental conductance characteristics are not as well-defined for trans-Si5 as for cis-Si5.

6. Analysis of junction structures and calculated transmissions

In the manuscript the transmission, junction lengths (Au—Au distance), and intramolecular distances (S—S and C—C distances) are analyzed for junctions with both Au—S—CH$_2$—Si dihedrals in ortho contact geometry (ortho/ortho). Here we complete

set of data for junctions with the anti/ortho and anti/anti contact geometries as well. All 490 junction structures are included as 3D-rotable web-enhanced objects in *xyz* file format. As discussed earlier in this section, we shall refrain from making direct comparison of results from junctions with different types of contact geometries.

Ortho/Ortho

In the manuscript the computational results are discussed and rationalized for the junctions with both terminal Au—S—CH_2—Si dihedrals in ortho configuration. In Figure 5b in the manuscript a couple of important trends can be seen. Most notably **cis-Si5** generally has a higher transmission than **trans-Si5** at any Au—Au distance. However, there is a general Au—Au distance dependence of the transmission: longer junctions systemically have lower transmissions. The systematic difference in transmission between **cis-Si5** and **trans-Si5** may be due to a systematic difference in the backbone dihedrals.

In Figure S11, we analyze the dihedrals of the 165 junctions with ortho/ortho contact geometry. In the top plot, the transmission at the Fermi energy is plotted against the backbone and linker dihedrals. There is no systematic trend indicating that **cis-Si5** should have more favorable dihedrals for conductance than **trans-Si5**. Similar to the vacuum structures, the C—Si—Si—Si dihedrals spread across a wider range for **cis-Si5** than **trans-Si5**, and some junctions for **cis-Si5** have more favorable dihedrals. However, this is a weak and somewhat unsystematic trend. As the junction length systematically influences the transmission, we plot the backbone and linker dihedrals against the Au—Au distance of the junction in Figure S11 bottom plot. Again there is no clear indication that **cis-Si5** has more favorable backbone dihedrals for junctions of the same length.
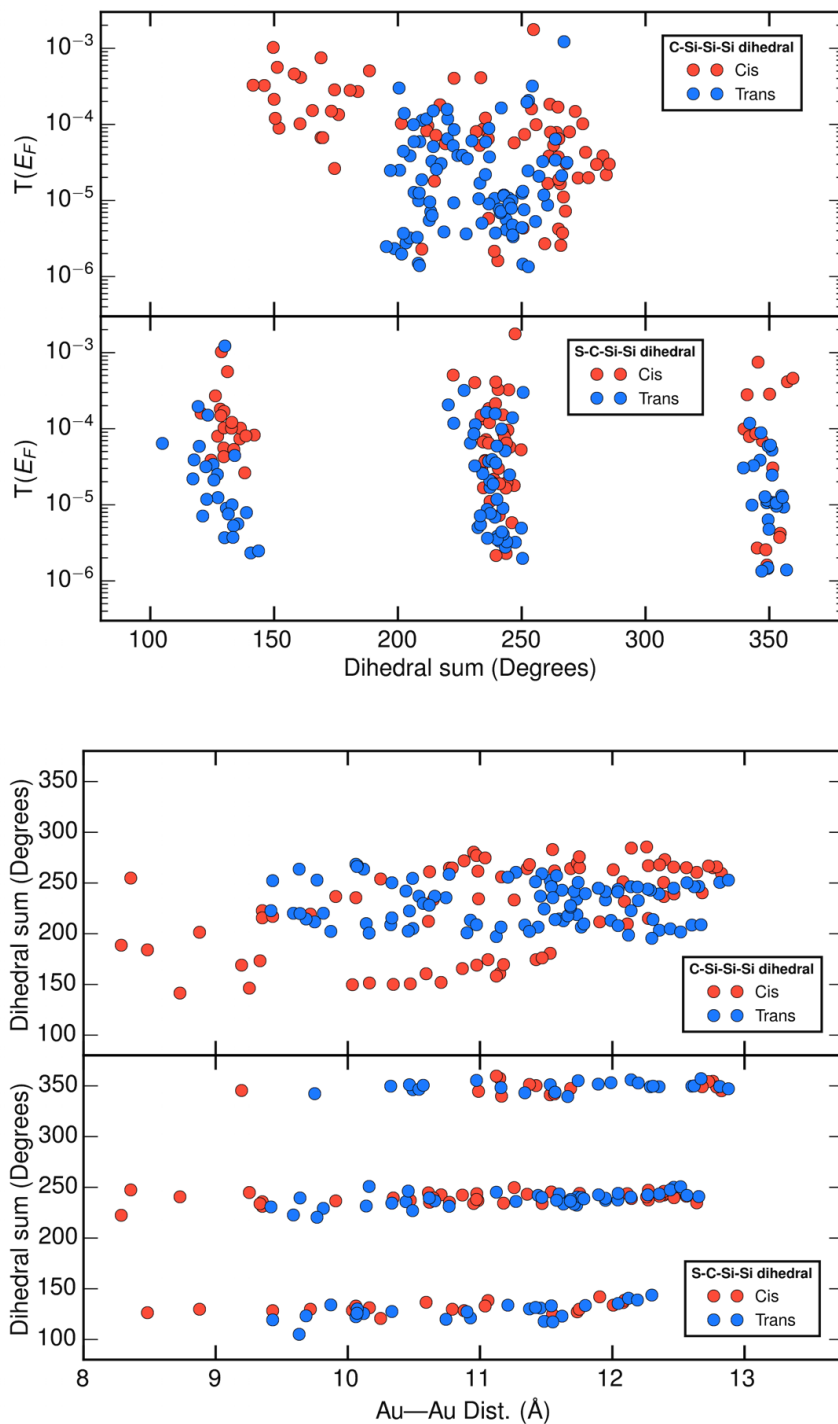
Figure S11: *Backbone dihedrals of 165 junctions with ortho/ortho contact geometry.* ***Top:*** *Transmission at the Fermi energy plotted against the sum of the two C—Si—Si(CH₂)₂—Si dihedrals (top) and the sum of the two S—C—Si—Si dihedrals (bottom).* ***Bottom:*** *Sum of the two C—Si—Si(CH₂)₂—Si dihedrals (top) and sum of the two S—C—Si—Si dihedrals (bottom) plotted against the Au—Au distance of the junctions.*

Anti/Ortho

We then investigate the 238 junctions with the two terminal Au—S—CH$_2$—Si dihedrals in anti and ortho configuration respectively. The results are analyzed and plotted the same way as for the ortho/ortho results. Figure S12 corresponds to Figure 5 in the manuscript, and Figure S13 corresponds to Figure S11.

In Figure S12a, we show the transmission histograms based on the vacuum population of the conformers. Both **trans-Si5** and **cis-Si5** have peaks with very low transmission, which does not correspond to the peaks in the experimental conductance histograms. Notably, similar to Figure 5a in the manuscript, **cis-Si5** does have a number of junctions with transmission in the range of the high conductance peak seen in experiment just below $10^{-3} \cdot G_0$. In Figure S12b the transmission at Fermi energy is plotted against the Au—Au distance of the junction. Here we see a number of **cis-Si5** junctions that have short Au—Au distances with high transmission. Both **trans-Si5** and **cis-Si5** have a wide range distribution of transmissions. The intramolecular distances plotted in Figure S12c show that the S—S and C—C distances are fairly similar for **trans-Si5** and **cis-Si5**. The main difference is that **trans-Si5** does not form short junctions with this contact geometry (with the algorithm we have used here).
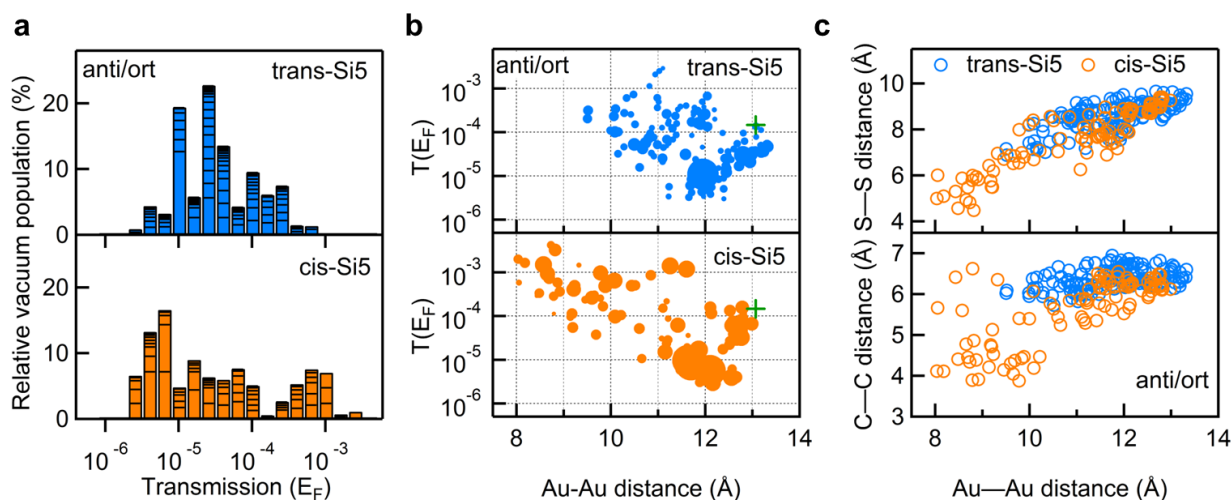

Figure S12: Transmission data of 140 ***trans-Si5*** *and 98* ***cis-Si5*** *with terminal Au—S—CH$_2$—Si dihedrals in anti/ortho contact geometry. (a) Logarithmically binned histogram of transmission at Fermi energy. The horizontal stack lines in the bars indicate the vacuum population of each conformer. The histogram is normalized to sum up to 100%. (b) Transmission at Fermi energy plotted against the Au—Au junction distance for each* ***trans-Si5*** *and* ***cis-Si5*** *conformer bridged between four-atom Au pyramids. The size of each dot scales with 1/(1+E), where E is the relative vacuum energy of each conformer in units of kT, see table S1 and S2. Green + is the calculated transmission for linear Si3 with one electrode in ortho and the other in anti conformation. (c) S—S (upper panel) and C—C junction*

*distance (lower panel) plotted against the Au—Au junction distance for each **trans-Si5** and **cis-Si5** conformer. S refers to sulfur; C refers to the CH₂-group that bridges between the silicon ring and the methylsulfide group. All three plots share the same color scale: orange for cis-Si5 and blue for **trans-Si5**.*

There is no clear difference in the trends of the transmissions of **trans-Si5** and **cis-Si5** with anti/ortho contact geometry. The same is true for the dihedrals of these junctions as well, shown in Figure S13.
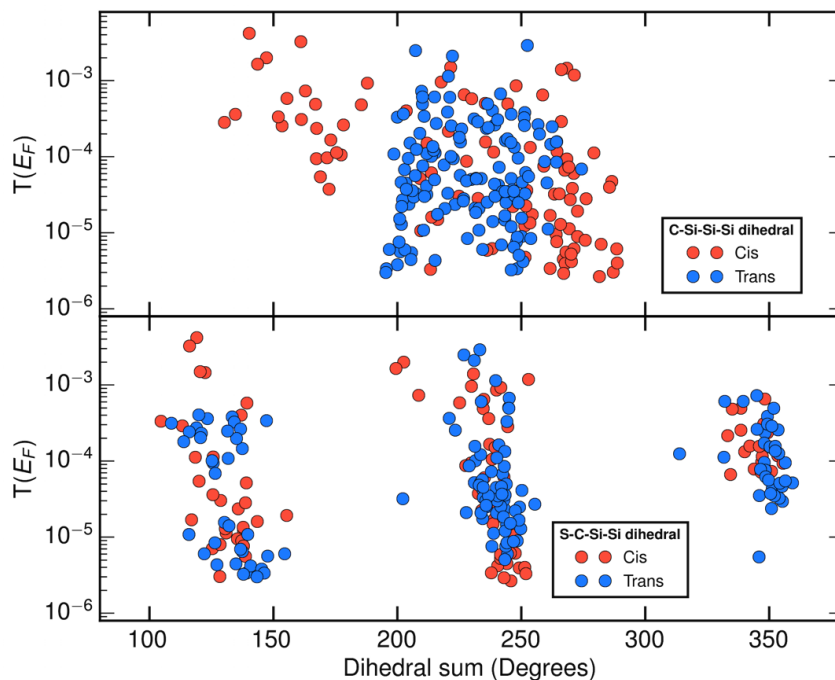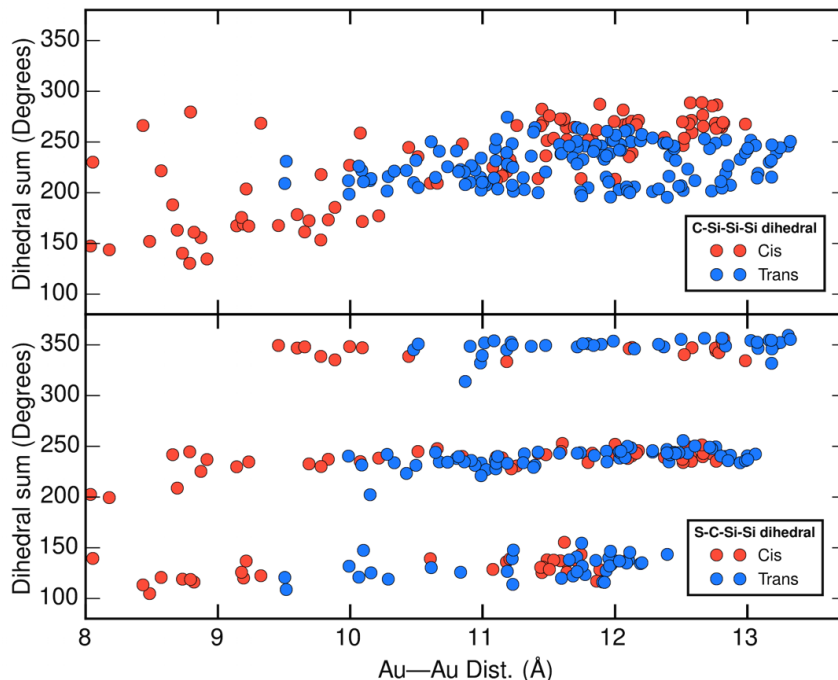
Figure S13: *Backbone dihedrals of 238 junctions with anti/ortho contact geometry. Top: Transmission at the Fermi energy plotted against the sum of the two C—Si—Si(CH₂)₂—Si dihedrals (top) and the sum of the two S—C—Si—Si dihedrals (bottom). Bottom: Sum of the two C—Si—Si(CH₂)₂—Si dihedrals (top) and sum of the two S—C—Si—Si dihedrals (bottom) plotted against the Au—Au distance of the junctions.*

Anti/Anti

Finally, we show the results for the 87 junctions with both the terminal Au—S—CH₂—Si dihedrals in anti configuration. In Figure S14a both **trans-Si5** and **cis-Si5** have a high transmission peak (High-G) that corresponds to systems with favorable backbone dihedrals, but also share high-populated lower transmission peaks (Low-G). We note that both the High-G and Low-G of **cis-Si5** are higher than the ones for the **trans-Si5**.
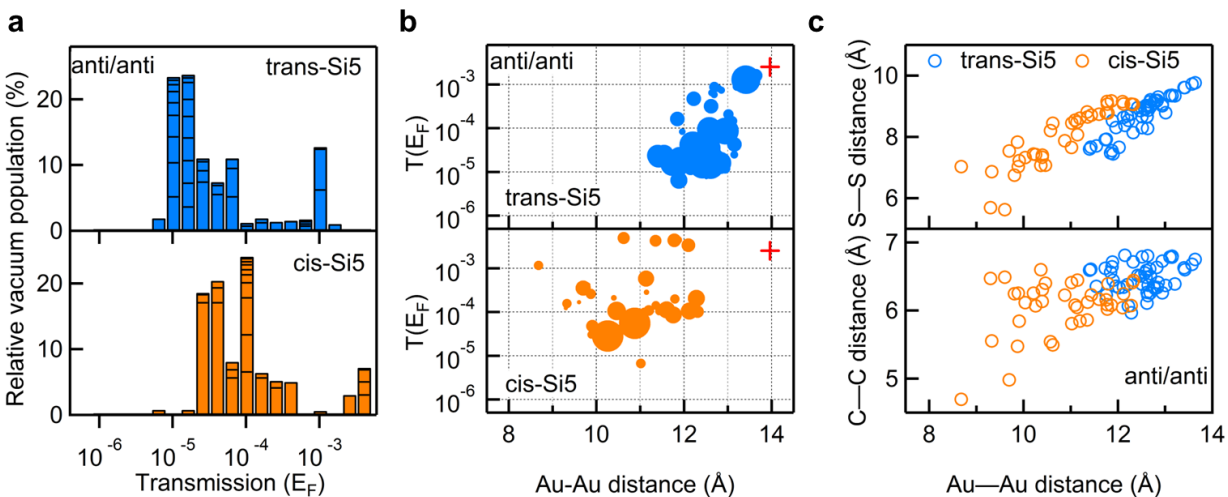
Figure S14: *Transmission data of 48* **trans-Si5** *and 39* **cis-Si5** *with terminal Au—S—CH₂—Si dihedrals in anti/anti contact geometry. (a) Logarithmically binned histogram of transmission at Fermi energy. The horizontal stack lines in the bars indicate the vacuum population of each conformer. The histogram is normalized to sum up to 100%. (b) Transmission at Fermi energy plotted against the Au—Au junction distance for each* **trans-Si5** *and* **cis-Si5** *conformer bridged between four-atom Au pyramids. The size of each dot scales with $1/(1+E)$, where E is the relative vacuum energy of each conformer in units of kT, see table S1 and S2. Red + is the calculated transmission for linear Si3 with both electrodes in anti conformation. (c) S—S (upper panel) and C—C junction distance (lower panel) plotted against the Au—Au junction distance for each* **trans-Si5** *and* **cis-Si5** *conformer. S refers to sulfur; C refers to the CH₂-group that bridges between the silicon ring and the methylsulfide group. All three plots share the same color scale: orange for* **cis-Si5** *and blue for* **trans-Si5***.*

Looking at the correlation between junction length and transmission at Fermi energy in Figure S14b, we notice that both **trans-Si5** and **cis-Si5** show a range of transmission values where the longer junctions generally have higher transmissions. This is because the backbone dihedrals of the molecule are more important to the transmission when the molecule is in the strongly coupled anti/anti contact geometry. These geometries may not be fully captured in the experiment, because although some conductance traces of **cis-Si5** show high conductance for extended (long) junctions, no or very few traces of **trans-Si5** show an extended (long) junction with this high conductance. But as mentioned earlier, we believe the anti/anti contact geometry, in contrary to the linear systems, is not very important for cyclic Si5**.**

The backbone and linker dihedrals in Figure S15 show no clear difference between **trans-Si5** and **cis-Si5**. It is worth noting that **cis-Si5** can form many shorter junctions — this is not a matter of the dihedrals but of the general structure of the molecule and the algorithm we use for determining if a junction structure is feasible. The long junctions with high transmission are conformers with favorable backbone and linker dihedrals.
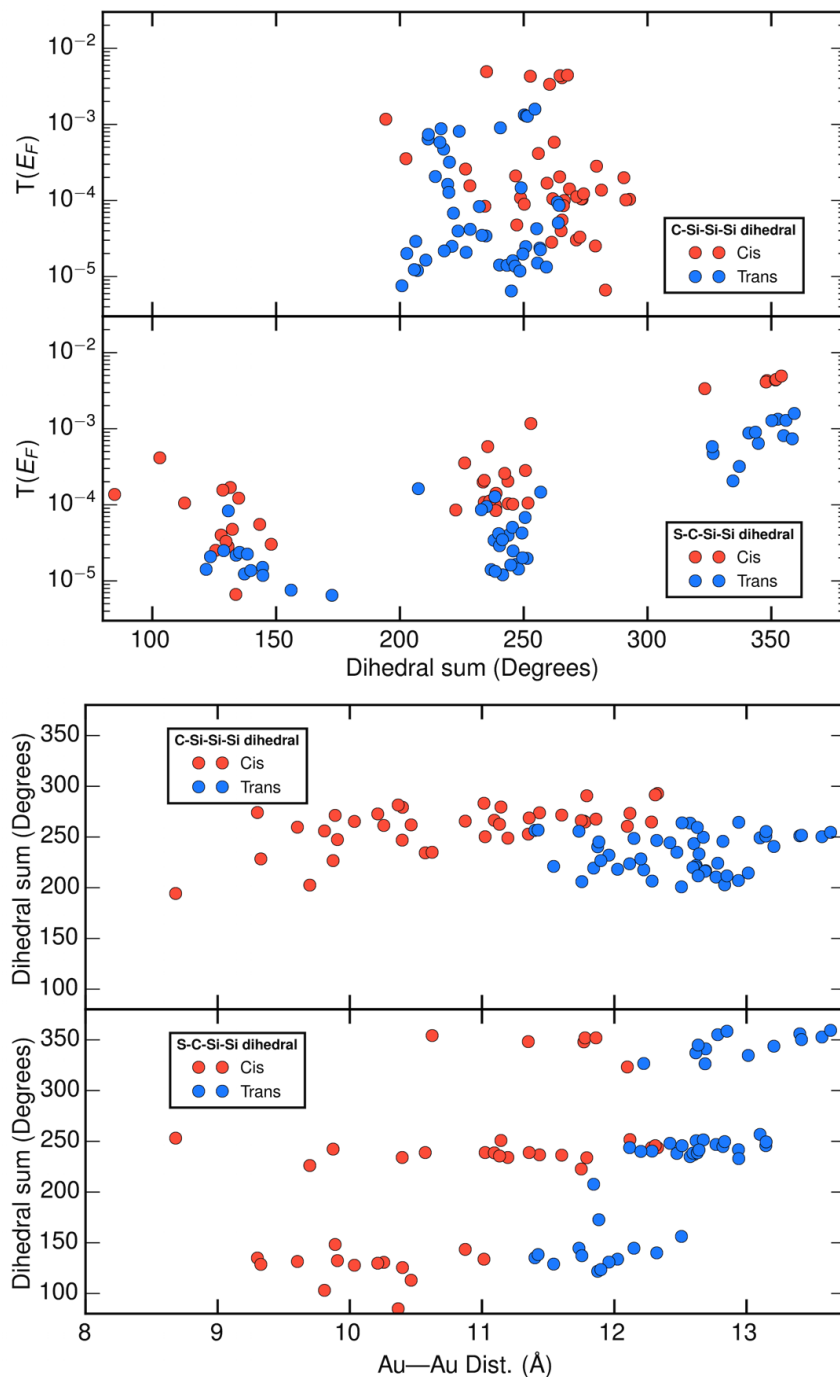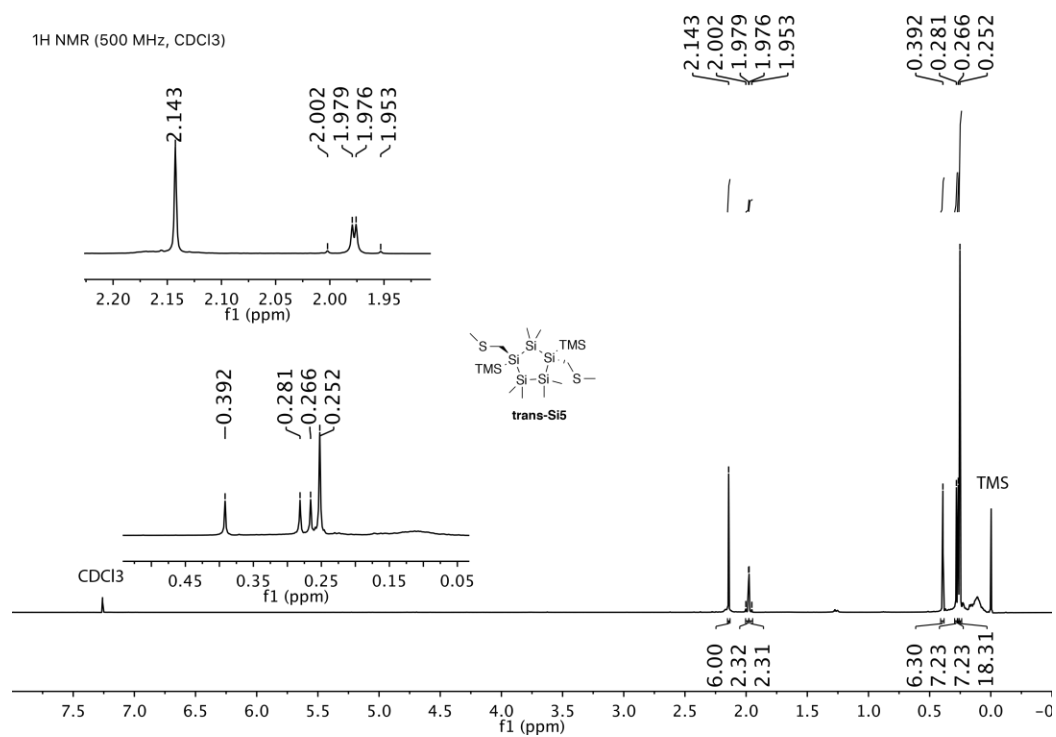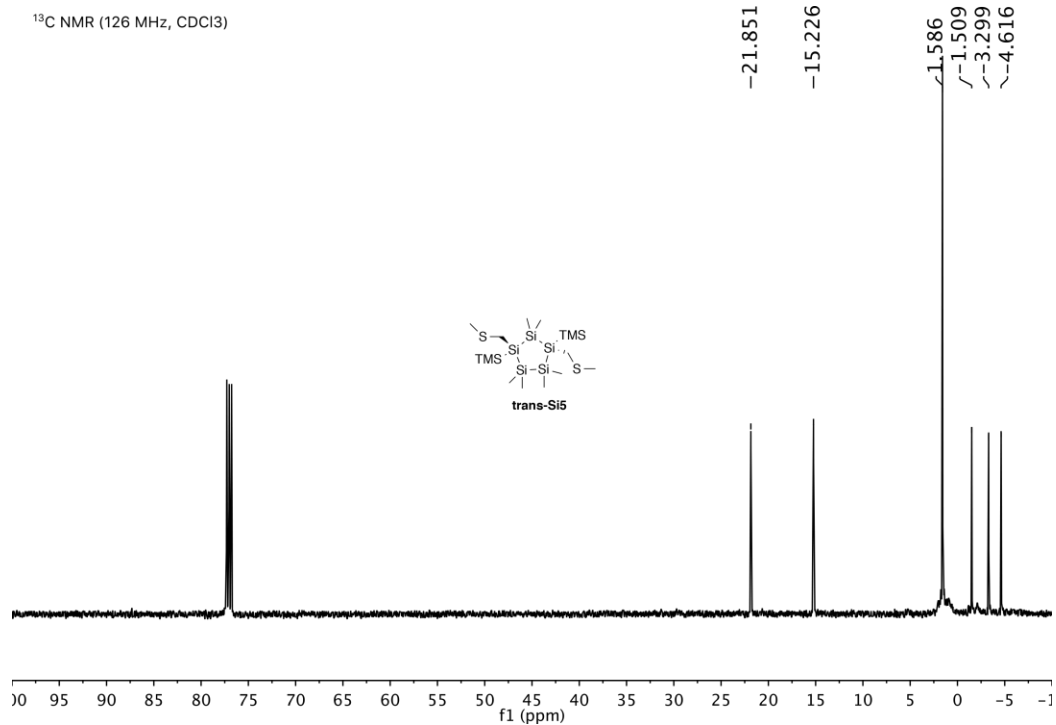
Figure S15*: Backbone dihedrals of 87 junctions with anti/anti contact geometry. Top: Transmission at the Fermi energy plotted against the sum of the two C—Si—Si(CH₂)₂—Si dihedrals (top) and the sum of the two S—C—Si—Si dihedrals (bottom). Bottom: Sum of the two C—Si—Si(CH₂)₂—Si dihedrals (top) and sum of the two S—C—Si—Si dihedrals (bottom) plotted against the Au-Au distance of the junctions.*
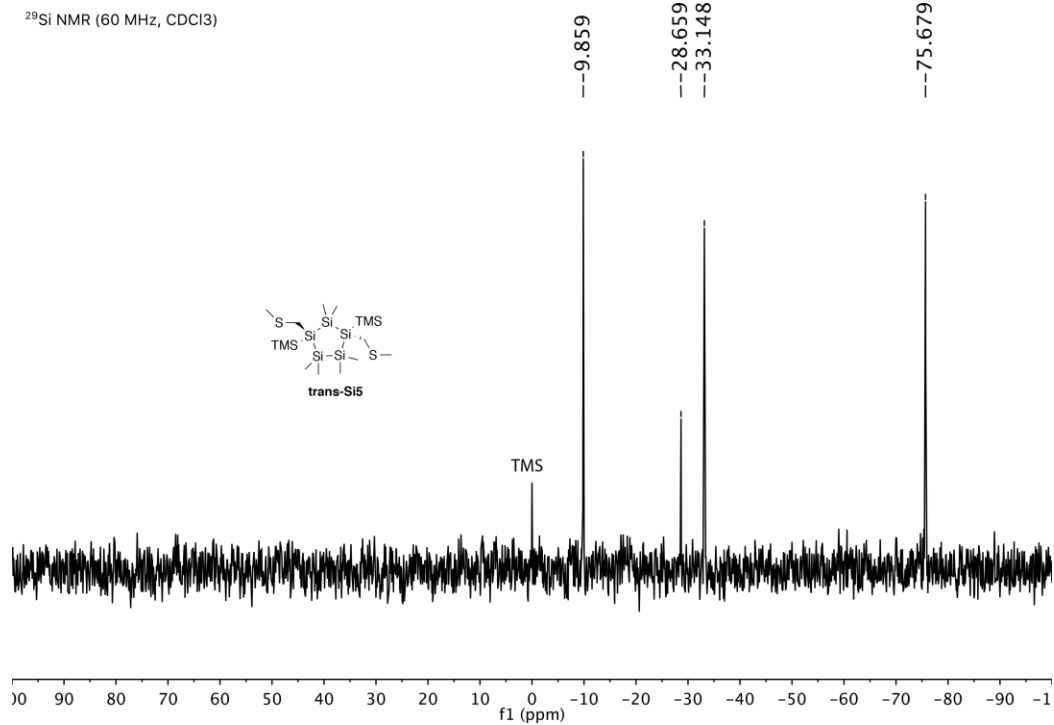
V. NMR spectra for trans-Si5 and cis-Si5

¹H NMR of **trans-Si5**

1H NMR (500 MHz, CDCl3)

2.143
2.002
1.979
1.976
1.953

0.392
0.281
0.266
0.252

2.20 2.15 2.10 2.05 2.00 1.95
f1 (ppm)

−0.392
0.281
0.266
0.252

trans-Si5

TMS

CDCl3 0.45 0.35 0.25 0.15 0.05
f1 (ppm)

6.00
2.32
2.31

6.30
7.23
7.23
18.31

7.5 7.0 6.5 6.0 5.5 5.0 4.5 4.0 3.5 3.0 2.5 2.0 1.5 1.0 0.5 0.0 −0
f1 (ppm)

¹³C NMR of **trans-Si5**

13C NMR (126 MHz, CDCl3)

−21.851

−15.226

1.586
−1.509
−3.299
−4.616

trans-Si5

00 95 90 85 80 75 70 65 60 55 50 45 40 35 30 25 20 15 10 5 0 −5 −1
f1 (ppm)

33

^{29}Si NMR of **trans-Si5**

^{29}Si NMR (60 MHz, CDCl3)

−9.859

−28.659
−33.148

−75.679

TMS

trans-Si5

f1 (ppm)

^{1}H NMR of **cis-Si5**

^{1}H NMR (500 MHz, CDCl$_3$)

2.162
2.078
2.055
2.047
2.025

0.450
0.334
0.282
0.236
0.229

TMS

cis-Si5

CDCl3

6.00
1.97
1.88

2.86
6.12
3.67
17.01
5.76

f1 (ppm)

34

^{13}C NMR of cis-Si5

^{13}C NMR (126 MHz, CDCl3)

77.160

−22.058

−15.450

1.753
−0.449
−2.220
−3.392
−4.304

cis-Si5

TMS

00 95 90 85 80 75 70 65 60 55 50 45 40 35 30 25 20 15 10 5 0 −5 −1
f1 (ppm)

^{29}Si NMR of cis-Si5

^{29}Si NMR (60 MHz, CDCl3)

−0.000

−9.656

−28.606
−32.678

−74.867

cis-Si5

TMS

140 120 100 80 60 40 20 0 −20 −40 −60 −80 −100 −120 −140
f1 (ppm)

VI. Single crystal X-ray diffraction

Data for all compounds was collected on an Agilent SuperNova diffractometer using mirror-monochromated Cu Kα or Mo Kα radiation. Data collection, integration, scaling (ABSPACK) and absorption correction (face-indexed Gaussian integration[15] or numeric analytical methods[16]) were performed in CrysAlisPro.[17] Structure solution was performed using ShelXS,[18] ShelXT,[19] or SuperFlip.[20] Subsequent refinement was performed by full-matrix least-squares on F^2 in ShelXL.[18] Olex2[21] was used for viewing and to prepare CIF files. PLATON[22] was used extensively for SQUEEZE,[23] ADDSYM[24] and TwinRotMat. Many disordered solvent molecules were modeled as rigid fragments from the Idealized Molecular Geometry Library.[25] Thermal ellipsoids are rendered at the 50% probability level.

Cis-Si5 was first dissolved in diethyl ether with gentle heating. The solution was then brought to room temperature and stored at -30°C overnight. White crystals of **Cis-Si5** were obtained which were then sent for X-ray diffraction and further analysis.
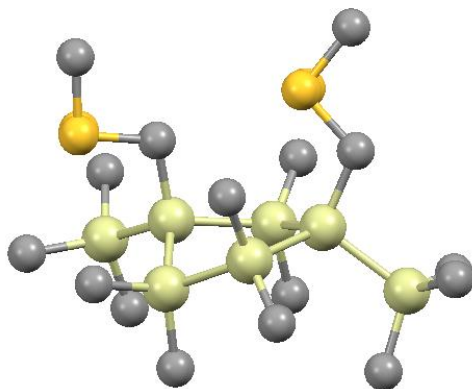

Figure S16. *Molecular structure of cis-Si5. Hydrogen atoms are omitted for clarity. Gray: carbon; green: Silicon; Yellow: Sulfur.*

Empirical formula	$C_{16}H_{46}S_2Si_7$
Formula weight	499.28
Temperature/K	293(2)
Crystal system	triclinic
Space group	P-1
a/Å	9.1609(3)
b/Å	10.5066(3)
c/Å	16.4935(4)
α/°	74.609(2)
β/°	82.416(2)
γ/°	81.240(2)
Volume/Å^3	1505.72(8)
Z	2
ρ_{calc}g/cm^3	1.101
μ/mm^{-1}	4.277
F(000)	544.0
Crystal size/mm^3	0.2 × 0.1 × 0.1
Radiation	CuKα (λ = 1.54184)
2Θ range for data collection/°	8.796 to 156.304
Index ranges	-9 ≤ h ≤ 11, -12 ≤ k ≤ 12, -20 ≤ l ≤ 20
Reflections collected	44944
Independent reflections	5896 [R_{int} = 0.1342, R_{sigma} = 0.0635]
Data/restraints/parameters	5896/0/240
Goodness-of-fit on F^2	1.331
Final R indexes [I>=2σ (I)]	R_1 = 0.0655, wR_2 = 0.1617
Final R indexes [all data]	R_1 = 0.0736, wR_2 = 0.1773
Largest diff. peak/hole / e Å^{-3}	1.26/-0.83

VII. References:

1.   M. G. Assadi and N. Golipour, Main Group Chemistry **5** (3), 179-190 (2006).

2.   S. M. Whittaker, M. Brun, F. Cervantes-Lee and K. H. Pannell, Journal of Organometallic Chemistry **499** (1), 247-252 (1995).

3.   R. Fischer, D. Frank, W. Gaderbauer, C. Kayser, C. Mechtler, J. Baumgartner and C. Marschner, Organometallics **22** (18), 3723-3731 (2003).

4.   T. A. Blinka and R. West, Organometallics **5** (1), 128-133 (1986).

5.   M. Hanwell, D. Curtis, D. Lonie, T. Vandermeersch, E. Zurek and G. Hutchison, Journal of Cheminformatics **4** (1), 17 (2012).

6.   T. A. Halgren, Journal of computational chemistry **17** (5‐6), 490-519 (1996).

7.   T. A. Halgren, Journal of Computational Chemistry **17** (5‐6), 520-552 (1996).

8.   T. A. Halgren, Journal of Computational Chemistry **17** (5‐6), 553-586 (1996).

9.   T. A. Halgren and R. B. Nachbar, Journal of Computational Chemistry **17** (5‐6), 587-615 (1996).

10.   T. A. Halgren, Journal of Computational Chemistry **17** (5‐6), 616-641 (1996).

11.   A. Tkatchenko and M. Scheffler, Physical Review Letters **102** (7), 073005 (2009).

12.   H. A. Fogarty, C.-H. Ottosson and J. Michl, Journal of Molecular Structure **556** (1–3), 105-121 (2000).

13.   C.-H. Ottosson and J. Michl, The Journal of Physical Chemistry A **104** (15), 3367-3380 (2000).

14.   T. A. Su, H. Li, M. L. Steigerwald, L. Venkataraman and C. Nuckolls, Nat Chem **7** (3), 215-220 (2015).

15.   E. Blanc, D. Schwarzenbach and H. D. Flack, Journal of Applied Crystallography **24** (6), 1035-1041 (1991).

16.   R. C. Clark and J. S. Reid, Acta Crystallographica Section A **51** (6), 887-897 (1995).

17.   O. D. CrysAlisPRO, Yarnton, England Search PubMed (2011).

18.   G. Sheldrick, Acta Crystallographica Section A **64** (1), 112-122 (2008).

19.   G. Sheldrick, Acta Crystallographica Section C **71** (1), 3-8 (2015).

20.   L. Palatinus and G. Chapuis, Journal of Applied Crystallography **40** (4), 786-790 (2007).

21.   O. V. Dolomanov, L. J. Bourhis, R. J. Gildea, J. A. K. Howard and H. Puschmann, Journal of Applied Crystallography **42** (2), 339-341 (2009).

22.   A. Spek, Acta Crystallographica Section D **65** (2), 148-155 (2009).

23.   P. van der Sluis and A. L. Spek, Acta Crystallographica Section A **46** (3), 194-201 (1990).

24.   Y. Le, Journal of Applied Crystallography **21** (6), 983-984 (1988).

25.   I. Guzei, Journal of Applied Crystallography **47** (2), 806-809 (2014).